Thermoelectric Transport Properties of Fe-Enriched ZnO with High-Temperature Nanostructure Refinement

Xin Liang*,‡

School of Engineering and Applied Sciences, Harvard University, Cambridge, Massachusetts 02138, United States

ABSTRACT: Thermoelectric properties of Fe-doped ZnO materials are investigated and correlated with the phase and microstructural evolution. Both a ZnO solid solution phase and a $ZnFe_2O_4$ spinel phase are observed. Analysis was made of temperature measurements of Seebeck coefficients as combined with the law of mixture to estimate the Fermi level in the constituent phases, which are further correlated with the Fe solute concentration in ZnO lattices and the overall electrical conductivity. In addition, the thermoelectric figure of merit is found to increase with the actual Fe content in ZnO lattices, due to the reduced thermal conductivity by point defect scattering of phonons and enhanced electrical transport via electron doping. The maximum achievable power factor of Fe-doped ZnO material is found to be similar to that of the ZnO–In_2O_3 system. Another important finding of the present work is the significant nanostructure refinement in 18 month old $FeO_{1.5}$-doped ZnO after high-temperature thermal treatment, leading to further reduced thermal conductivity, which is beneficial and promising for high-temperature thermoelectric performance.

KEYWORDS: thermoelectrics, oxide, grain refinement, nanostructure
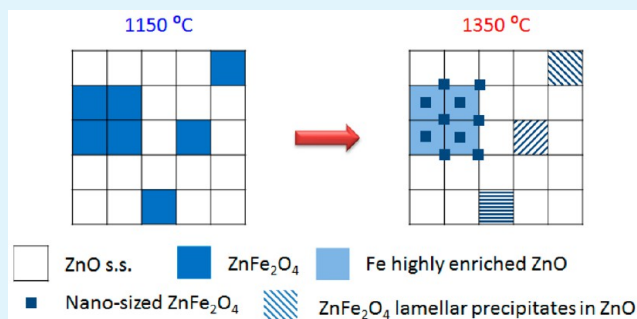
INTRODUCTION

ZnO-based oxide system has a rich variety of doping choices on altering the microstructure as well as tuning the transport properties. Examples of dopant elements are Al,[1,2] Bi,[3] Co,[4] In,[5–9] Fe,[10,11] Mn,[12] Ni,[13,14] Sb,[15] Sn,[16] and even dual doping.[17–19] This research provides useful information on the doping effect on the structure and/or properties, while it lacks a systematic investigation of the thermoelectric properties, especially with combined observation on the microstructure. The Fe-doped ZnO system is one such example not yet deeply explored, especially on thermoelectric transport properties. Light doping of Fe into ZnO was found not to cause any change of microstructure.[20,21] Nevertheless, there were a few works on Fe highly doped ZnO reporting the formation of oxide defect structure including inversion domain structure[11] or antiphase modulated structure,[10] both of which are in the length scale of 10 nm. However, few systematic efforts have been made to explore the thermoelectric properties of Fe-doped ZnO; neither the thermal conductivity nor the electrical conductivity and the Seebeck coefficient have been investigated. It is of primary interest in the present work to look into the effect of phase equilibria and microstructure on thermoelectric properties of Fe-doped ZnO.

In the present work, 2, 4, and 18 month-old (m/o) $FeO_{1.5}$-doped ZnO, with pure ZnO as reference, were synthesized to obtain different phase equilibria and investigate the thermo-electric properties. The 2 and 4 m/o $FeO_{1.5}$-doped ZnO were annealed at 1250 °C for achieving the solid solution phase. The 18 m/o $FeO_{1.5}$-doped ZnO was annealed at 1150 and 1350 °C

to reach different phase equilibria and microstructures, including a two-phase microstructure and a highly Fe-concentrated ZnO solid solution phase. The compositions and heat treatment temperatures of samples are indicated on the ZnO–$FeO_{1.5}$ binary phase diagram shown in Figure 1a, which was adapted from Degterov et al.'s work.[22]

EXPERIMENTAL SECTION

The oxide powders were prepared with a wet-chemistry gel-combustion combined approach. High-purity commercial nitrate powders $Zn(NO_3)_2$ (99.999%, Sigma-Aldrich, USA) and $Fe(NO_3)_3$ (99.99%, Sigma-Aldrich, USA) were dissolved in deionized and distilled water. After determination of ionic concentrations, each solution was weighed and mixed according to the iron concentration. The mixed solution was uniformly stirred and held at 80 °C. With addition of a few organic fuels (acrylamide, N,N′-methylene-bis(acrylamide), 2,2′-azobisisobutyro-nitrile, and ammonium persul-fate), the liquid solution was converted into the gel, which was then dried in a low-temperature oven at 120 °C for 12 h to remove the water. The dried gel was crushed into small pieces and sent into combustion furnace in which self-assisted reaction occurred at ~600 °C. The combustion powders were then calcined at 800 °C for 2 h to remove the carbon and other residual organic chemicals. After being finely ground, the calcined powders were then sintered into solid pellets using current-assisted densification processing system (also known as spark plasma sintering) at 900 °C for 5 min. During the entire sintering process, the powders were under vacuum with a
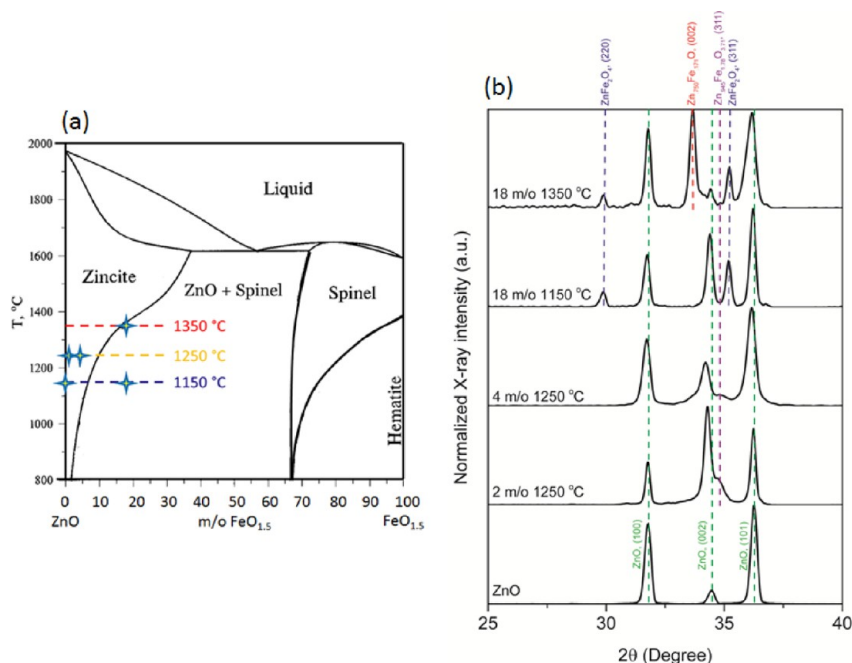
Figure 1. Phase equilibrium of ZnO–FeO$_{1.5}$ binary system. (a) Phase diagram adapted from Degterov et al.'s work.[22] Sample compositions and annealing temperatures are indicated on the figure. (b) X-ray diffraction results of Fe-doped ZnO with pure ZnO data also presented. Characteristic peaks of each phase are labeled.

compressive stress of 125 MPa. The sintered solid samples were postannealed in air furnace to achieve different phase equilibria and microstructures. As a reference, pure ZnO was sintered in the same way and further annealed in air at 1150 °C for 1 d.

X-ray diffraction analysis was performed at a Bruker D8 Discover Diffractometer. The phases were analyzed and identified with 2011 ICDD PDF database.[23] The cross sections of samples were ground and polished to 1 μm followed by the thermal etching at 1050 °C for 30 min for scanning electron microscopy (SEM) imaging and elemental analysis, which was performed on a Zeiss Super VP55 FEG-SEM with X-ray energy dispersive spectroscopy (EDS). Transmission electron microscopy (TEM) investigations were also made to look into the evolution of microstructure. Specimens were prepared in a conventional method of mechanical thinning followed by ion beam milling on a Fischione 1010 Dual Beam Ion-Mill machine. After the samples were further cleaned on a Fischione 110 Plasma Cleaner, the TEM observations were made on JEOL 2010 FEG-TEM. Scanning transmission electron microscopy (STEM) with X-ray EDS mapping analysis was also made in the purpose of understanding the elemental distribution of fine structures, which was conducted on a Cs-aberration corrected Zeiss Libra 200 MC STEM with twin EDS detectors.

Thermal conductivity (κ) was obtained from the thermal diffusivity (α), which was measured from room temperature to 800 °C in flowing argon gas on a NETZCH Micro Flash LFA 457 instrument. Heat capacity C_p was calculated using the Kopp–Neumann rule from literature data,[24] and the mass density ρ was measured using Archimedes method. The thermal conductivity with temperature was then determined from the relation

$$\kappa(T) = \alpha(T)\cdot\rho\cdot C_p(T) \tag{1}$$

Specimens were cut into bars of dimensions ~2 × 2 × 8 mm for electrical conductivity and Seebeck coefficient measurements, which were made in air from room temperature to 800 °C on a ULVAC RIKO ZEM 3 M 10 unit.

■ RESULTS

Structural Characterization. X-ray diffraction results for Fe-doped ZnO, including pure ZnO as reference, are presented in Figure 1b. The X-ray scan of all the samples was made from

2θ of 10° to 70°, while spectra in the range of 2θ of 25° to 40° are presented as they are most representative of important phase and structure features. Characteristic peaks of each phase are labeled. Analysis of the X-ray diffraction results reveals several important features, as will be described in the following.

With increasing Fe concentration to 4 m/o FeO$_{1.5}$, a systematic shift of ZnO (002) peak toward smaller 2θ angle was observed, which indicates increasing basal plane spacing, implying an increased incorporation of Fe ions into the ZnO lattice. A continuous broadening of ZnO (101) peaks with increasing Fe concentration was also observed, as has also been reported in literature.[25] In addition, a ZnFe$_2$O$_4$-type of spinel phase (cubic, $Fd\bar{3}m$) but deficient in Fe, one example of which is a Zn$_{0.945}$Fe$_{1.78}$O$_{3.71}$ phase (ICDD No. 01−079−1500), was found to be present in both 2 and 4 m/o FeO$_{1.5}$-doped ZnO that were annealed at 1250 °C. The 4 m/o FeO$_{1.5}$-doped ZnO seems to have a smaller fraction of Zn$_{0.945}$Fe$_{1.78}$O$_{3.71}$ spinel phase than the 2 m/o FeO$_{1.5}$ sample, but it has larger concentration of Fe in ZnO lattice, as seen from the larger shift of ZnO (002), (100), and (101) peaks.

The X-ray diffraction results shown in Figure 1b suggest the presence of both ZnO and ZnFe$_2$O$_4$ spinel phases in 18 m/o FeO$_{1.5}$-doped ZnO annealed at 1150 °C, which is expected from the phase diagram shown in Figure 1a. However, it is interesting that ZnO solid solution phase possesses a lower content of Fe, as clearly seen from its smaller shift of ZnO (002) peak as compared to that of 2 or 4 m/o FeO$_{1.5}$-doped ZnO. The volume fraction of spinel phase was estimated to be ~0.18. After the 18 m/o FeO$_{1.5}$ sample was further annealed at 1350 °C for 3 d, two ZnO solid solution phases were identified. One ZnO solid solution phase has the (002) peak close to the pure ZnO one, whereas the other one has a significant shift and identified as the (002) peak of Zn$_{0.750}$Fe$_{0.171}$O, an Fe highly enriched ZnO solid solution phase (ICSD No. 155784).[25] In addition, a tiny amount of Fe-deficient ZnFe$_2$O$_4$ spinel phase was also observed in addition to the stoichiometric ZnFe$_2$O$_4$
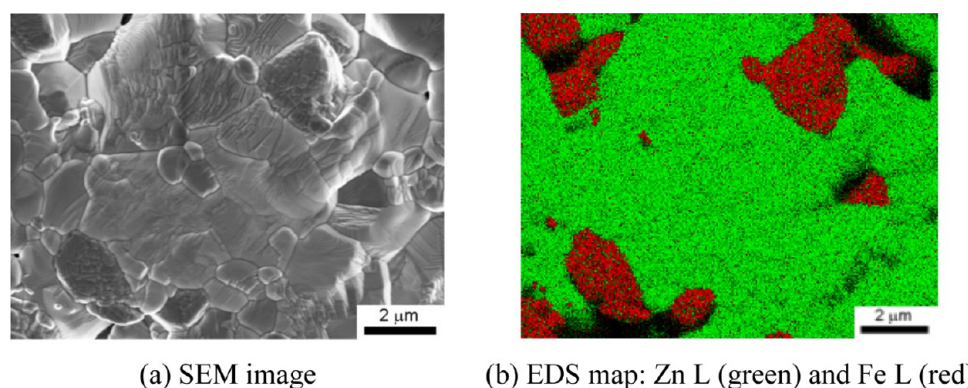
(a) SEM image   (b) EDS map: Zn L (green) and Fe L (red)

Figure 2. Cross-section microstructure of 18 m/o $FeO_{1.5}$-doped ZnO annealed at 1150 °C for 1 d: (a) SEM micrograph; (b) EDS mapping with green and red colored data points representing Zn and Fe, respectively.
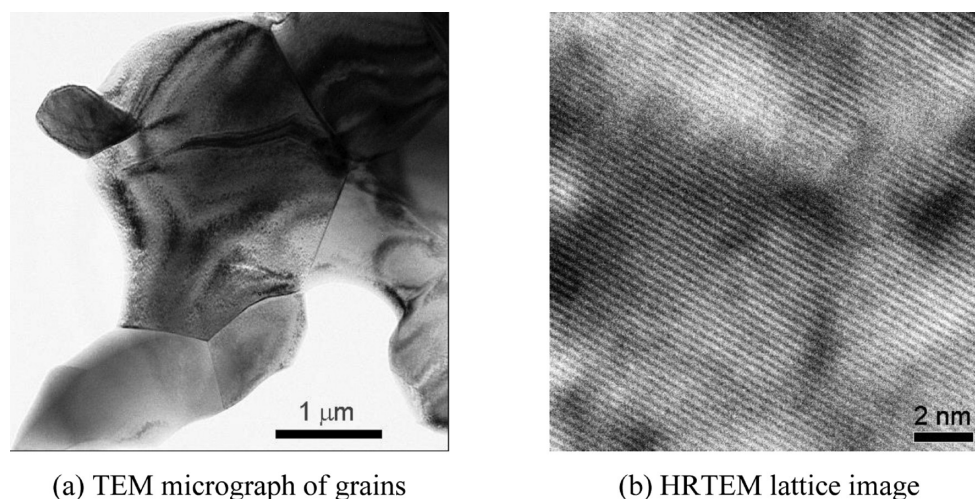
(a) TEM micrograph of grains   (b) HRTEM lattice image

Figure 3. TEM observations of microstructure in 18 m/o $FeO_{1.5}$-doped ZnO annealed at 1150 °C for 1 d: (a) TEM micrograph of grains; (b) HRTEM lattice image of ZnO {002} basal planes.
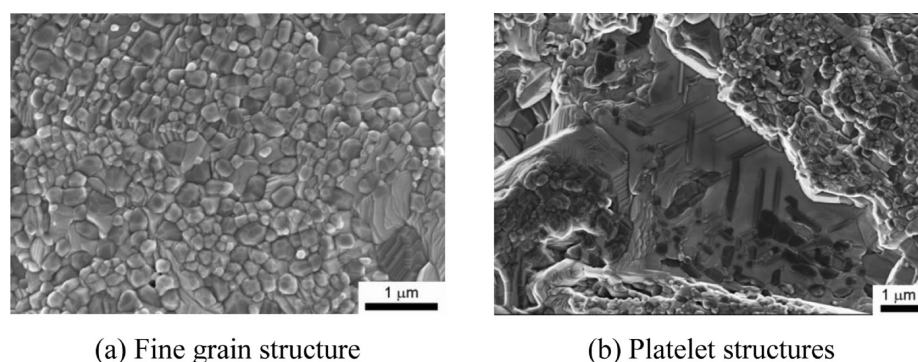
(a) Fine grain structure   (b) Platelet structures

Figure 4. SEM micrographs of cross-section microstructure of 18 m/o $FeO_{1.5}$-doped ZnO annealed at 1350 °C for 3 d. (a) Fine grain structures. (b) Platelet or lamellar structures.

spinel phase. Another feature found in this sample is the peak broadening, especially the ZnO (101) peak, indicating the reduction in grain size.

The 18 m/o $FeO_{1.5}$-doped ZnO, with plenty of features revealed by the X-ray diffraction, was further investigated under electron microscopy. The SEM cross-section micrograph of the sample after 1150 °C annealing is shown in Figure 2a. The typical grain size was ~2−3 μm. The corresponding EDS elemental mapping, as presented in Figure 2b, suggests the presence for ZnO solid solution phase and $ZnFe_2O_4$ spinel

phase, as is consistent with the X-ray diffraction results. The grain structure is clean inside as shown in the TEM micrograph in Figure 3a. In addition, no oxide defect structures such as superlattice interfaces or antiphase boundaries were observed in our high-resolution (HR) TEM investigations; one typical lattice image of ZnO {002} basal planes is presented in Figure 3b.

After a further annealing at 1350 °C for 3 d, a significant structural change in 18 m/o $FeO_{1.5}$ sample was observed, as shown in the SEM observations in Figure 4. The material
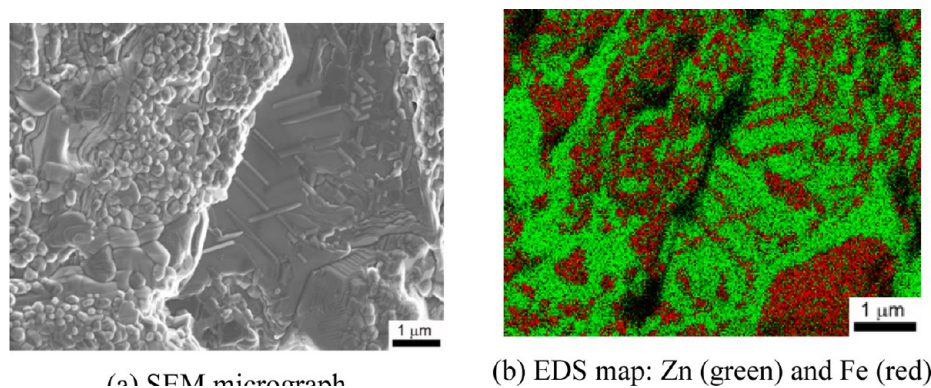
(a) SEM micrograph

(b) EDS map: Zn (green) and Fe (red)

Figure 5. Cross-section microstructure of 18 m/o FeO$_{1.5}$-doped ZnO annealed at 1350 °C for 3 d. (a) SEM image. (b) EDS mapping with green and red colored data points representing Zn and Fe, respectively.
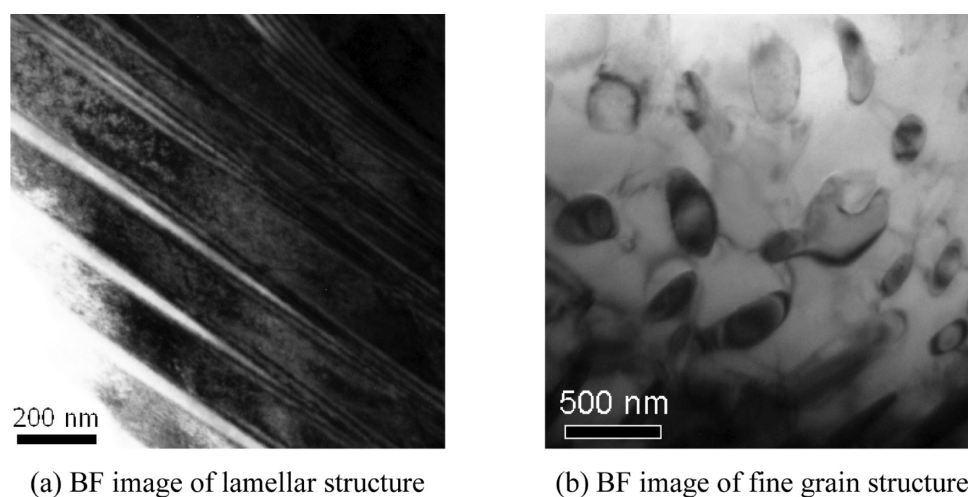

(a) BF image of lamellar structure

(b) BF image of fine grain structure

Figure 6. Bright field TEM micrographs of typical microstructures in 18 m/o FeO$_{1.5}$-doped ZnO annealed at 1350 °C for 3 d: (a) lamellar and (b) fine grain structures.

evolves into two types of structures. One is fine grain structure with grain size reduced to ~200 nm, as shown in Figure 4a; the other is platelet or lamellar-type structure embedded in a large grain as shown in Figure 4b. The SEM and the corresponding EDS elemental map in Figure 5a,b, which captures both types of structures, suggest that these fine grains and platelets are Fe-rich phases and therefore are the ZnFe$_2$O$_4$ spinel phase that was identified by X-ray diffraction analysis. Performing an imaging analysis of the EDS mapping gives a volume fraction of 0.17 for ZnFe$_2$O$_4$ spinel phase. The phase compositions and fractions in 18 m/o FeO$_{1.5}$ sample remain virtually unchanged between the two thermal treatments, whereas the microstructure and morphology have undergone a significant evolution.

TEM investigations observed on ZnO {002} planes revealed more details of the lamellar or platelet structures in the 18 m/o FeO$_{1.5}$ sample annealed at 1350 °C, as show in Figure 6a. Although there are a few reports of the presence of superlattice structure (SL) or inverse domain boundaries (IDBs) in Fe-doped ZnO where Fe−O layers or IDBs stack along c-axis of the ZnO,[10,11,26−29] no such structures or related defect contrast were observed in this material even in our extensive HRTEM observations of ZnO {002} planes. In addition, it is noted that the average platelet spacing is ~200 nm, which is much larger than the average superlattice or IDB spacing, which is only a few nm. Furthermore, the platelet is much thicker than the superlattice interface or IDBs, which are only one to two atomic

layers thick. Fine grain structures of a few hundred nanometers in size, as seen in the SEM micrograph in Figure 4a, were also observed under TEM, as shown in Figure 6b.

A further STEM EDS elemental map was made for ZnO {002} planes, as shown in Figure 7, suggesting that the thin lamellar structures are enriched in Fe and therefore in the ZnFe$_2$O$_4$ spinel phase, while the matrix is a ZnO solid solution phase. A line scan profile is presented in Figure 7c, which provides semiquantitative information on the Fe and Zn distribution in a direction perpendicular to the platelet structure. Since the scan was taken from the edge of the specimen toward inside, as indicated by the arrow on the image in Figure 7a, the specimen thickness increases away from the edge, leading to the increasing energy dispersive analysis of X-rays signal intensity for both zinc and iron. The counts ratio of Fe to Zn across these thin Fe-rich platelets is ~2, which basically corresponds to the Fe/Zn ratio in ZnFe$_2$O$_4$ spinel compound. In addition, it is found that ZnFe$_2$O$_4$ platelets grow out of ZnO obeying the previously reported crystallographic orientation relationship of ZnFe$_2$O$_4$(111)[110]//ZnO(0001)-[11$\bar{2}$0].[30] The STEM EDS elemental map was also made on the fine grain structures as shown in Figure 8. Elemental distribution results clearly show that these fine grains, which have the grain size of ~200 nm, are ZnFe$_2$O$_4$ spinel phase embedded in the ZnO solid solution matrix.
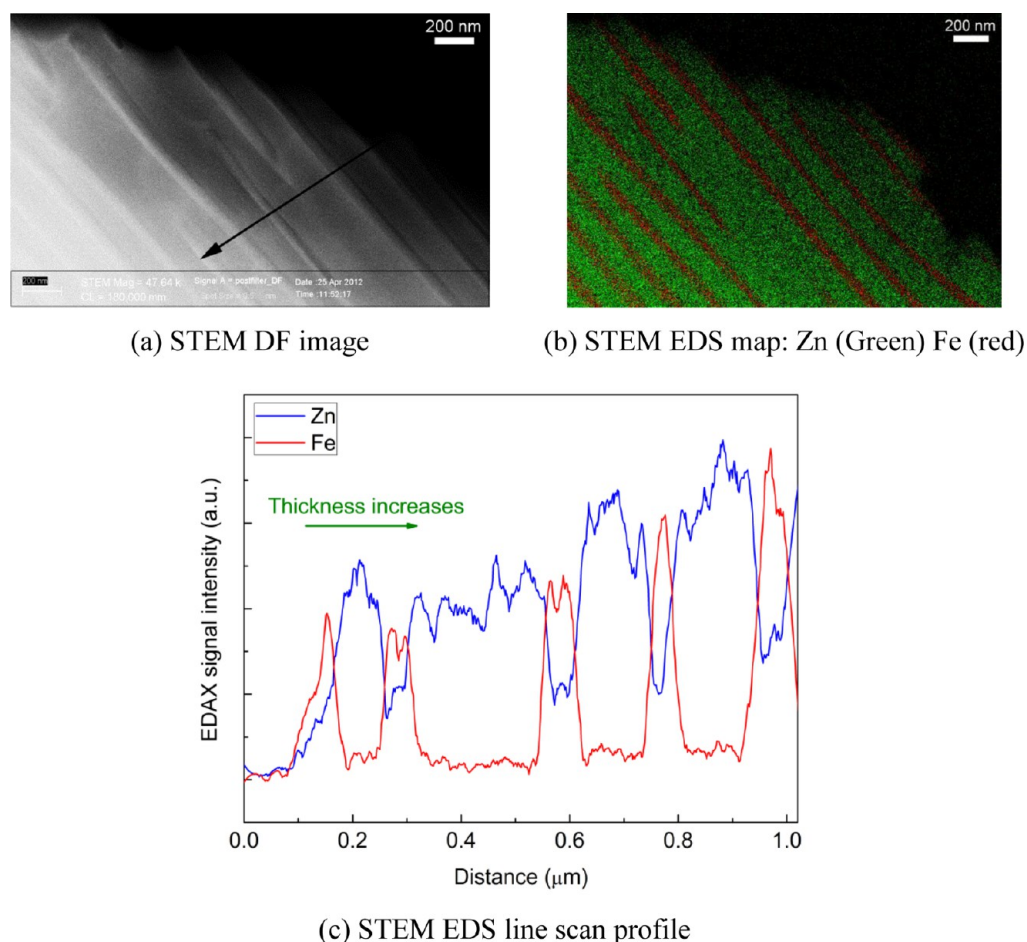
(a) STEM DF image

(b) STEM EDS map: Zn (Green) Fe (red)

(c) STEM EDS line scan profile

Figure 7. STEM image and elemental mapping of lamellar structure in 18 m/o FeO$_{1.5}$-doped ZnO annealed at 1350 °C for 3 d. (a) STEM dark field image with an arrow showing the line scan direction; (b) STEM EDS map with Zn and Fe represented by green and red colored data points, respectively; (c) STEM EDS line scan across several platelets showing the Zn and Fe profile. Clearly, the thin lamellar structures are highly enriched in Fe, and the ratio of Fe to Zn is ∼2, in correspondence with ZnFe$_2$O$_4$ spinel phase.
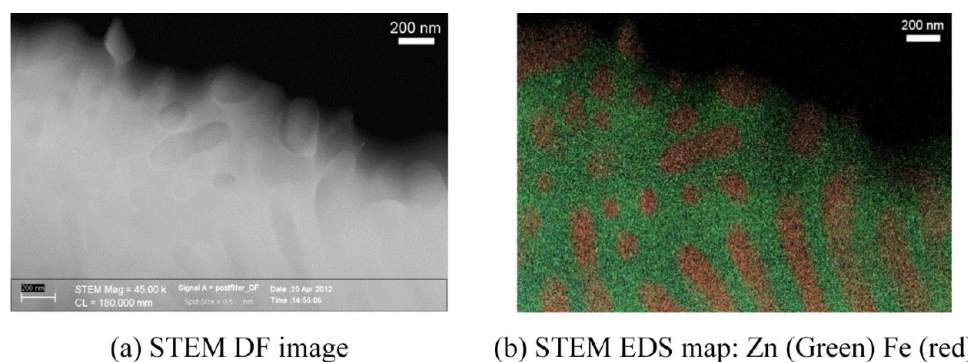

(a) STEM DF image

(b) STEM EDS map: Zn (Green) Fe (red)

Figure 8. Aberration-corrected STEM image and elemental mapping of fine grain structures in 18 m/o FeO$_{1.5}$-doped ZnO annealed at 1350 °C for 3 d. (a) STEM dark field image; (b) STEM EDS map with Zn and Fe represented by green and red colored data points, respectively.

Thermal and Electrical Transport Properties. Measured thermal conductivities of Fe-doped ZnO with temperature up to 800 °C are presented in Figure 9a. Doping ZnO with Fe results in both a significant drop in thermal conductivity as well as a reduced temperature dependence. It is also interesting to see that the 18 m/o Fe O$_{1.5}$ sample annealed at 1150 °C has higher thermal conductivity than the 2 or 4 m/o Fe O$_{1.5}$ samples, which are less Fe-doped; however, a further annealing at 1350 °C reduces the thermal conductivity by a factor of more than 2.

Electrical conductivity and Seebeck coefficient measurement results with temperature are presented in Figure 9b,c, respectively. Electrical conductivity of ZnO is significantly improved by Fe doping. In addition, for all the Fe-doped ZnO, electrical conductivity increases with temperature. The 18 m/o FeO$_{1.5}$ sample annealed at 1350 °C has the highest electrical conductivity, followed by the 4 m/o and 2 m/o FeO$_{1.5}$ samples annealed at 1250 °C and the 18 m/o FeO$_{1.5}$ sample annealed at 1150 °C. For all the samples, Seebeck coefficient has exactly the opposite trend as that of electrical conductivity, namely, the
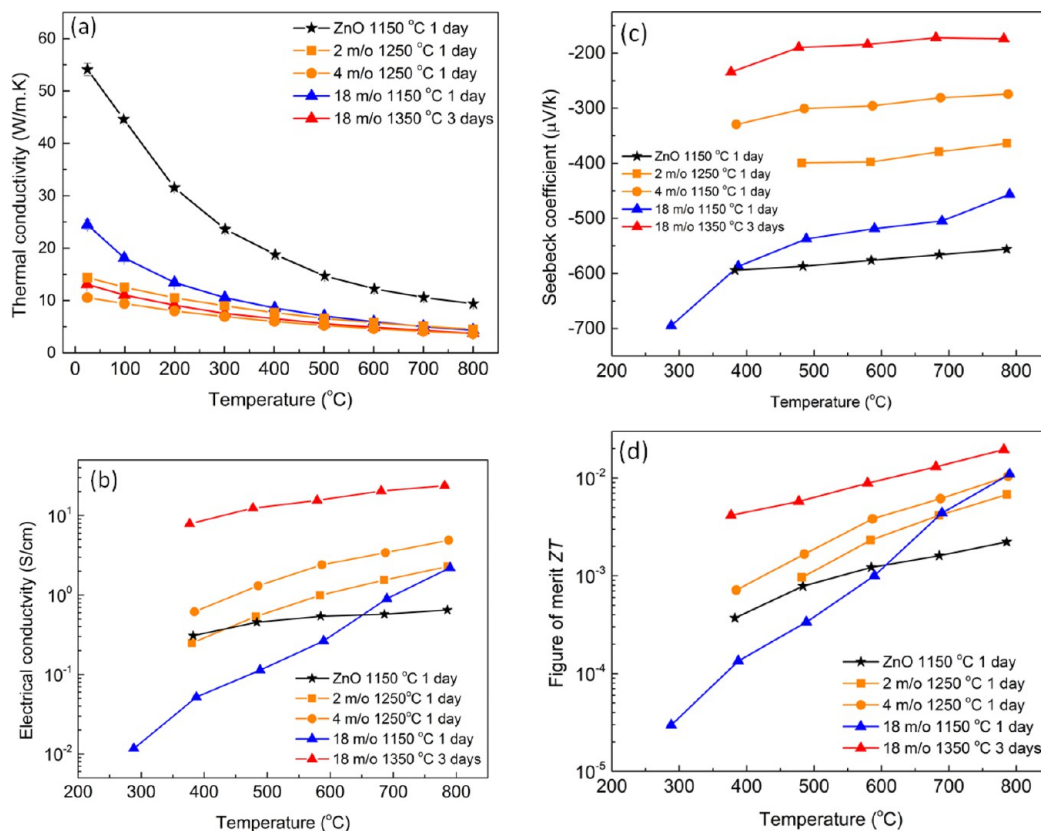
Figure 9. Thermal conductivity (a), electrical conductivity (b), Seebeck coefficient (c), and figure of merit ZT (d) of Fe-doped ZnO samples measured from room temperature to 800 °C. The solid lines are for visual guide.

sample that demonstrates high electrical conductivity has small Seebeck coefficient. These findings suggest that all these samples are of typical free electron semiconductors.

■ DISCUSSIONS

Phase Equilibria and ZnO Solid Solution. At relatively low Fe concentration, such as 2 and 4 m/o FeO$_{1.5}$, the phase diagram shown in Figure 1a predicts the single ZnO phase. However, in addition to the ZnO solid solution phase, our X-ray diffraction analysis also suggests the formation of a Zn$_{0.945}$Fe$_{1.78}$O$_{3.71}$ phase, which is an Fe-deficient ZnFe$_2$O$_4$ spinel phase. As FeO$_{1.5}$ doping increases from 2 to 4 m/o, we observed a reduced fraction of Fe-deficient ZnFe$_2$O$_4$ spinel phase and a ZnO solid solution phase that has higher Fe concentration, suggesting a competition between the phase stabilities of ZnO and ZnFe$_2$O$_4$ spinel phases. The formation of Fe-deficient ZnFe$_2$O$_4$ spinel phase possibly occurs during cooling when passing through the ZnO/(ZnO + spinel) phase boundary, when some of Fe ions left oversaturated ZnO and formed Fe-deficient spinel phase that is energetically favored at lower temperature.

Interesting phase change was found in the 18 m/o FeO$_{1.5}$-doped ZnO. When further annealed at 1350 °C and then cooled to room temperature, two ZnO solid solution phases with apparently different Fe concentrations were formed. The Fe highly concentrated ZnO, Zn$_{0.750}$Fe$_{0.171}$O, which has a much larger fraction than the less Fe concentrated ZnO solid solution phase, was not found in the sample annealed at 1150 °C nor in the 2 or 4 m/o FeO$_{1.5}$ sample. This is attributed to the fact that equilibrated at 1350 °C, the 18 m/o FeO$_{1.5}$ composition is nearly at the phase boundary reaching the large solubility limit

of Fe ions in ZnO lattices, as seen in the phase diagram in Figure 1a. Both stoichiometric and Fe-deficient spinel phase formed in this sample, but the Fe-deficient spinel phase only has a small fraction. It is clear from the X-ray diffraction results that both low Fe concentrated ZnO and Fe-deficient spinel are minor phases. Considering 2 and 4 m/o FeO$_{1.5}$ sample (annealed at 1250 °C) consists of both less Fe concentrated ZnO and Fe-deficient spinel phase, it is highly possible that the less Fe concentrated ZnO solid solution phase in the 18 m/o FeO$_{1.5}$ sample (1350 °C) was formed during cooling when the Fe solubility in ZnO lattice decreases and that equilibrium favors ZnO with less Fe content. The formation of a small amount of Fe-deficient spinel phase is also expected to occur during cooling and follow the similar scenario as of 2 or 4 m/o FeO$_{1.5}$ sample, which was discussed previously. Detailed discussions on the phase and microstructure evolution in the 18 m/o FeO$_{1.5}$ sample will be given in next section.

To evaluate the lattice parameter with the Fe concentration of the ZnO solid solution phase, the ZnO (002) basal plane spacing or $(c/2)$, where c is the unit cell lattice parameter, was obtained and calculated from the peak fitting of each X-ray diffraction data and plotted against m/o FeO$_{1.5}$ in Figure 10a. Referring to the phase diagram in Figure 1a, the 2 and 4 m/o FeO$_{1.5}$ compositions equilibrated at 1250 °C fall in the ZnO solid solution regime. Accordingly, it is reasonable to assume the lattice parameter of these two samples with that of pure ZnO follow the Vegard's law, which suggests a linear dependence of lattice parameter with solute concentration.[31] Together with the undoped ZnO, a straight line can be fitted through the data representing the Vegard's law prediction, as shown by the dashed green line on the figure. Imposing the
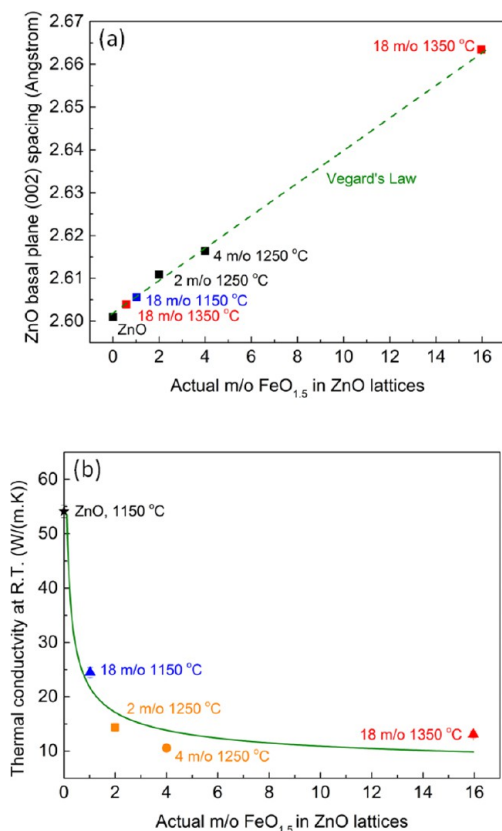
Figure 10. Effect of actual Fe content in ZnO lattices on the thermal conductivity. (a) ZnO basal plane (002) spacing or ($c/2$) measured by X-ray diffraction plotted as a function of actual m/o $FeO_{1.5}$ in ZnO lattices. The Vegard law was determined based on the undoped ZnO and the 2 and 4 m/o $FeO_{1.5}$-doped ZnO. The actual Fe content of ZnO solid solution in 18 m/o $FeO_{1.5}$ sample annealed at 1150 and 1350 °C was then estimated. (b) Room-temperature thermal conductivity of Fe-doped ZnO versus actual m/o $FeO_{1.5}$ in ZnO lattices. Each sample composition and annealing temperature is indicated beside the symbol. The solid green curve is the best fit of the measured data according to $\kappa \propto c^{-1/2}$.

ZnO (002) basal plane spacing or ($c/2$) of ZnO solid solution phases in the 18 m/o $FeO_{1.5}$ sample onto the Vegard's law, the actual Fe content in these solution phases can be estimated. The ZnO solid solution phase in the 18 m/o $FeO_{1.5}$-doped ZnO annealed at 1150 °C has only ∼1.0 m/o $FeO_{1.5}$ where much of Fe ions participate in the formation of $ZnFe_2O_4$ spinel phase. This can be attributed to the reducing Fe solubility with decreasing temperature. In the 18 m/o $FeO_{1.5}$-doped ZnO annealed at 1350 °C, ∼0.6 m/o $FeO_{1.5}$ content was estimated in the less Fe concentrated ZnO solution phase, which has a quite small fraction, whereas the Fe highly concentrated ZnO solid solution that is the major phase, is estimated to have ∼16.0 m/o $FeO_{1.5}$.

Microstructural Evolution of 18 m/o $FeO_{1.5}$ Sample. The microstructural and phase evolution of the 18 m/o $FeO_{1.5}$ sample annealed at 1150 and 1350 °C are relatively complicated but can be understood as a sequence of two major steps. The first step is the annealing at higher temperature, that is, at 1350 °C in the single-phase region. Clearly seen from the phase diagram in Figure 1a, as temperature increases from 1150 to 1350 °C, the two-phase mixture of ZnO solid solution phase and $ZnFe_2O_4$ spinel phase are transforming to a single ZnO solid solution phase with high

Fe concentration. The second step is cooling from 1350 °C to room temperature, during which a series of phase decomposition occurs, as seen from our X-ray diffraction and electron microscopy observations. As cooling starts, the major phase change is the precipitation of $ZnFe_2O_4$ spinel phase from the Fe highly enriched ZnO solid solution phase, obeying the (111) [110] // ZnO (0001)[11$\bar{2}$0] crystallographic relationship as observed from our electron microscopy studies. The EDS mapping of the 18 m/o $FeO_{1.5}$ sample annealed at 1350 °C suggests that the volume fraction of spinel phase is ∼0.17, and the corresponding molar faction is 0.09; this molar fraction relates to ∼1300 °C on the phase diagram according to the Lever rule. This finding also suggests that there was formation of ZnO solid solution phase with ∼13 m/o $FeO_{1.5}$ when cooled to this temperature. Nevertheless, a significant portion of Fe highly concentrated ZnO solid solution phase remained, which has ∼16.0 m/o $FeO_{1.5}$ as discussed previously.

As cooling continuously carries on, the Fe solubility in ZnO decreases and ZnO with less Fe content is favored by equilibrium. It turns out that a portion of ZnO solid solution phase changes to further lower Fe concentrated one. This is indicated by our X-ray diffraction result that the less Fe concentrated ZnO phase in the sample annealed at 1350 °C has only ∼0.6 m/o $FeO_{1.5}$. The Fe ions leave the ZnO solid solution phase and form the Fe-deficient spinel phase, as is the case of 2 or 4 m/o $FeO_{1.5}$ samples.

Such a series of phase decomposition and change yields one of the most interesting phenomena reported in the present work: the microstructure in the 18 m/o $FeO_{1.5}$ sample is significantly refined into nanoscale after high-temperature treatment (1350 °C), which is counterintuitive to the high-temperature coarsening phenomenon commonly observed in most ceramic materials.

With samples cooled from 1350 °C, the $ZnFe_2O_4$ spinel phase either develops into the morphology of lamellar or platelet structures obeying the (111)[110] // ZnO (0001) [11$\bar{2}$0] crystallographic relationship or precipitates as nano-grains with limited further growth due to the slowed diffusion process under cooling. Accordingly, original ZnO grains were then segmented into much smaller grains, and the average grain boundary spacing reduces by about an order of magnitude (from 2−3 μm to ∼200 nm).

Thermal Conductivity. To investigate the compositional and structural roles in thermal transport properties, the room-temperature thermal conductivity was plotted against the actual m/o $FeO_{1.5}$ in ZnO lattices as shown in Figure 10b. Fe addition and annealing temperature of each sample are indicated beside each symbol. As seen from the figure, thermal conductivity generally decreases with the actual Fe content in ZnO lattices, which can be attributed to the point defects introduced into the ZnO lattices and the microstructural refinement (the formation of lamellar $ZnFe_2O_4$ spinel structure). Point defects, which result in an atomic scale change, are normally more influential in affecting phonon transport. In the current case of doping Fe_2O_3 into ZnO, the defect reaction is given by[11]

$$Fe_2O_3 \xrightarrow{ZnO} 2Fe_{Zn}^{\bullet} + V_{Zn}'' + 3O_O^X + 3ZnO \tag{1}$$
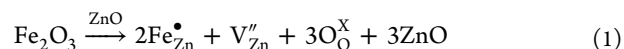
which suggests doping one molecule of Fe_2O_3 into ZnO creates two substitutional iron point defects on zinc sites and one zinc vacancy for charge balance. The chemical formula of ZnO with Fe introduced point defects is then written as

$$(Zn_{1-3c/2}Fe_cV_{c/2})O \qquad (2)$$

where c is the iron concentration. The point defect scattering strength factor Γ is characteristic of phonon scattering by point defects, and the general expression is given by[32]

$$\Gamma = \sum_i f_i\left(1 - \frac{M_i}{\overline{M}}\right)^2 \qquad (3)$$

where M_i is the mass of the defect and $\overline{M}$ is the average mass. In the current case, considering both the substitutional defects and zinc vacancy, Γ is written as

$$\Gamma = c\frac{(M_{Fe} - \overline{M_{Zn}})^2}{2(\overline{M_{ZnO}})^2} + \frac{c}{2}\frac{(\overline{M_{Zn}})^2}{(\overline{M_{ZnO}})^2} \qquad (4)$$

where $\overline{M_{ZnO}}$ is the mean mass of the doped ZnO formula unit and $\overline{M_{Zn}}$ is the average atomic mass on zinc site, both of which are dependent on iron concentration c. The first-order approximation in math gives

$$\Gamma \cong 0.67c \qquad (5)$$

This suggests an increasing point defect phonon scattering with increasing iron concentration Zn lattices. In addition, the thermal conductivity κ is inversely proportional to Γ.[33]

$$\kappa \propto \Gamma^{-1/2} \qquad (6)$$

This suggests that the thermal conductivity decreases with the Fe content c in the ZnO lattices, as seen by the best fit of the measured data, which is shown as a solid green curve in Figure 10b.

Thermoelectric Properties. Relating the actual Fe solute concentration with the electrical conductivity data, we find that the electrical conductivity in general increases with the actual Fe content in ZnO lattices. For instance, the 18 m/o FeO$_{1.5}$-doped ZnO sample annealed at 1350 °C, in which the ZnO solid solution phase has the largest Fe content among all the samples studied, demonstrates the highest electrical conductivity. This is especially true as temperature goes up when there are an increasing number of electrons delocalized from the donor defect states and excited to the conduction band, leading to a larger free charge carrier concentration n. The role of ZnFe$_2$O$_4$ spinel phase is unclear, but it is not a very poor electrical conductor based on its measured band gap of ~2.5 eV.[34]

A useful approach to look into the electrical transport process is to probe the relative position of the Fermi level in the band structure. Seebeck coefficient (also commonly known as thermopower or thermoelectric power in the literature), which is strongly related to the Fermi level in the materials,[35,36] can be used to investigate the electrical conduction processes in both bulk[35] and low-dimensional materials.[37−39] The Seebeck coefficient for an n-type semiconductor expressed in terms of Fermi level E_F as measured from the conduction band edge E_C is given by[36]

$$S = -\frac{k_B}{e}\left[\frac{E_C - E_F}{k_BT} + A_C\right] \qquad (7)$$

where e is the electronic charge and k_B is the Boltzmann's constant. A_C is a temperature-independent term named as the heat of transport constant, which is the contribution from the charge carriers that are distributed above the conduction band E_C.

$$A = \frac{\int_0^\infty \frac{E - E_C}{k_BT}\sigma(E)dE}{\int_0^\infty \sigma(E)dE}, \qquad E > E_C \qquad (8)$$

Considering the temperature dependence of bandgap and Fermi level, E_C and E_F in eq 7 can be replaced by $(E_C + \gamma_gT)$[40] and $(E_F + \gamma_FT)$,[37,39] respectively, where γ_g and γ_F are temperature coefficients for the change of bandgap and Fermi level with temperature. (In fact, in the cases of large doping or carrier concentration, the temperature dependence of Fermi level becomes quite weak.[41]) Accordingly, eq 7 can be rewritten as

$$-S = \frac{E_C - E_F}{e}\left(\frac{1}{T}\right) + A \qquad (9)$$

where $A = [((\gamma_g - \gamma_F/e) + A_C(k_B/e))]$. The above equation suggests that the Fermi level as measured from the conduction band edge can be estimated from the plot of $-S$ against $1/T$.

The Seebeck model in eq 9 assumes a single-phase material and therefore may be applied to ZnO, 2 m/o FeO$_{1.5}$, and 4 m/o FeO$_{1.5}$-doped ZnO in the present work. The modeling fit of the measured Seebeck coefficients as a function of temperature for these single-phase samples are presented in Figure 11a, where scattered symbols represent the measured data and dashed lines are modeling fit. The estimated Fermi levels are summarized in Table I. Our findings that the Fermi level is closer to the conduction band in the undoped sample can be attributed to native defects such as oxygen vacancies, which are commonly found in intrinsic ZnO.[31,42] From 2 to 4 m/o FeO$_{1.5}$ addition, we found a shift of Fermi level closer to the conduction band edge. This is consistent with the increased electrical conductivity because Fe ions are dissolved into ZnO lattices providing electron donors without forming the second phase.

Since 18 m/o FeO$_{1.5}$-doped ZnO samples are two-phase materials consisting of ZnO and ZnFe$_2$O$_4$ spinel phases, we need a model for describing the Seebeck behavior of a composite material on the dependence of each phase constituent. We can write the Seebeck coefficient of a two-phase material based on Bergman and Fel's model,[43] which describes the electrical conductivity and thermoelectric power factor of two-phase composite:

$$S = \frac{f_A\sigma_AS_A + (1 - f_A)\sigma_BS_B}{f_A\sigma_A + (1 - f_A)\sigma_B} \qquad (10)$$

where σ_i and S_i (i = A or B) represents the electrical conductivity and Seebeck coefficient of each phase, and f_A is the volume fraction of the phase A. The difficulty in applying Bergman's model is the unknown electrical conductivity of each phase, which can be significantly different from the intrinsic and undoped phase due to the electron doping in each phase. In practice, it is not a bad approach to apply the law of mixture in describing the Seebeck coefficient of a two-phase material; it has been reported that the law of mixture model on predicting Seebeck coefficient of a two-phase composite is a reasonably good estimation unless the electrical conductivity of the two phases differs by several orders of magnitude.[44] Accordingly, it is not a bad approximation to apply this practical approach to our material system. The Seebeck coefficient of the FeO$_{1.5}$ heavily doped ZnO, which consists of ZnO and ZnFe$_2$O$_4$ phases, is given by

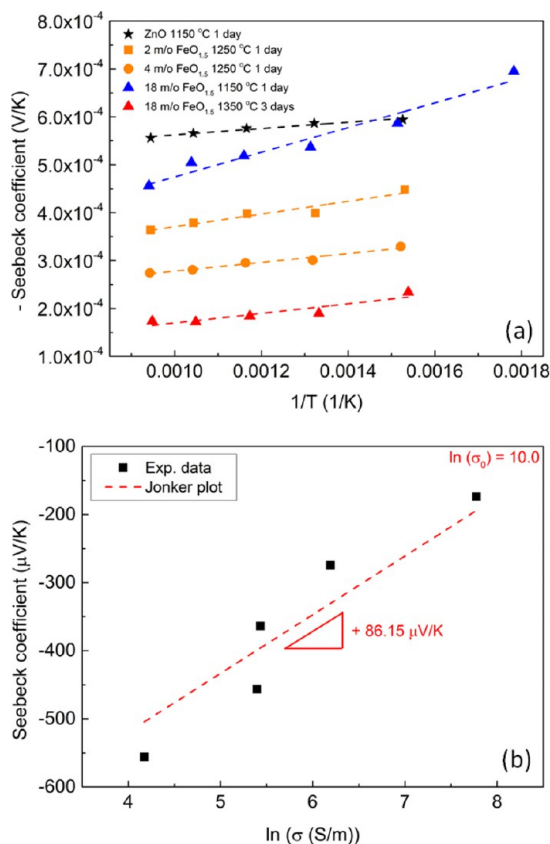$$S = f_{spinel}S_{spinel} + (1 - f_{spinel})S_{ZnO} \qquad (11)$$

Figure 11. Analysis of Seebeck coefficient of Fe-doped ZnO. (a) Plot of negative Seebeck coefficient ($-S$) against the inverse of absolute temperature $1/T$. Measured data are shown by the scattered symbols of different colors; dashed lines of the corresponding colors are the modeling fit of the experimental data according to eq 9 for single-phase samples (ZnO and 2 m/o and 4 m/o $FeO_{1.5}$-doped ZnO) and eq 11 for two-phase samples (18 m/o $FeO_{1.5}$ samples). (b) Jonker plot (Seebeck coefficient against natural logarithm of electrical conductivity) of Fe-doped ZnO (including pure ZnO) measured at 800 °C. The best fit of the data with a slope of +86.15 μV/K is shown as the dashed line.

Table I. Summary of Estimated Fermi Levels from the Temperature Dependent Seebeck Coefficient Measurements[a]

	f_{spinel}	$(E_C - E_F)_{ZnO}$, eV	$(E_C - E_F)_{ZnFe_2O_4}$, eV
ZnO, 1150 °C 1 d	0	0.066	
2 m/o $FeO_{1.5}$, 1250 °C 1 d	0	0.133	
4 m/o $FeO_{1.5}$, 1250 °C 1 d	0	0.092	
18 m/o $FeO_{1.5}$, 1150 °C 1 d	0.18	0.196	0.538
18 m/o $FeO_{1.5}$, 1350 °C 3 d	0.17	0.100	0.100

[a]The volume fractions of $ZnFe_2O_4$ spinel phase are also shown.

where S_{spinel} and S_{ZnO} are the Seebeck coefficients of $ZnFe_2O_4$ and ZnO phases, and f_{spinel} is the volume fraction of the $ZnFe_2O_4$ phase. S_{spinel} and S_{ZnO} can be further expressed using eq 7. Similar to the single phase model shown in eq 9, we plot the $-S$ of 18 m/o $FeO_{1.5}$ samples as a function of $1/T$, as shown by the scattered symbols in Figure 11a. The modeling fit of the measured data according to eq 11 are represented by the dashed lines, from which we estimated the Fermi levels in both ZnO and $ZnFe_2O_4$ phases, as also summarized in Table I. It is clearly found that the Fermi level in both phases is much closer

to the conduction band in the higher temperature annealed samples (1350 °C) as compared to the one annealed at 1150 °C. This is well consistent with the much higher Fe solute concentration observed in the higher temperature annealed sample (see Figure 10a) as well as its higher electrical conductivity (see Figure 9b). Also concluded from Table I, all the samples are nondegenerate semiconductors even with $FeO_{1.5}$ addition up to 18 m/o, as Fermi levels all lie below the conduction band.

We further perform the Jonker plot analysis through which the electrical conductivity is correlated with Seebeck coefficient.[45−47] Electrical conductivity σ for semiconductor materials is given by the standard equation

$$\sigma = ne\mu \qquad (12)$$

where e is the electronic charge and μ is the electron mobility. Seebeck coefficient function is already presented in eq 7. To make it explicitly correlated with electrical conductivity, we shall re-express it in terms of carrier concentration n. In semiconductors, carrier concentration is dependent on the Fermi level through the well-known relationship below (for n-type semiconductor)[48]

$$n = N_C \exp\left(-\frac{E_C - E_F}{k_B T}\right) \qquad (13)$$

where N_C is the density of states at the conduction band edge given by $N_c = (2\pi m_e^* k_B T/\hbar^2)^{3/2}$ in which m_e^* is the effective mass. Substituting eq 13 into eq 7, we can readily rewrite the Seebeck coefficient in terms of the carrier concentration.

$$S = -\frac{k_B}{e}\left[\ln\left(\frac{N_c}{n}\right) + A_C\right] \qquad (14)$$

Combining eqs 12 and 14, one immediately obtains the correlation equation between Seebeck coefficient and electrical conductivity.

$$S = \frac{k_B}{e}(\ln(\sigma) - \ln(\sigma_0)) \qquad (15)$$

where $\sigma_0 = N_c e\mu \exp(A)$. This suggests a linear behavior when the Seebeck coefficient is plotted against the natural logarithm of electrical conductivity, which is commonly known as a Jonker plot.[45]

As shown in Figure 11b, all our data measured at 800 °C were made in a Jonker plot, and a reasonably good correlation between electrical conductivity and Seebeck coefficient is obtained with a linear slope of +86.15 μV/K, corresponding to the Seebeck value of classical free electron gas k_B/e.[49] This suggests that the electrical conduction process in these Fe-doped ZnO materials are dominated by free electrons. The intercept, $\ln(\sigma_0)$, referred as "DOS-μ" product, was found to have a value of 10.0, very similar to the value of $ZnO-In_2O_3$ system.[50] In addition, Ioffe analysis[46,47,51] suggests that the maximum achievable thermoelectric power factor PF_{max} is dependent on $\ln(\sigma_0)$ given by the relation below.

$$\ln PF_{max} = \ln \sigma_0 + \ln 4\left(\frac{k_B}{e}\right)^2 - 2 \approx -19.33 + \ln \sigma_0 \qquad (16)$$

This gives the $PF_{max} \approx 0.9 \times 10^{-4}$ W/mK², which is a reasonably good value for oxide materials.

The thermoelectric figure of merit ZT is calculated according to standard relation

$$ZT = \frac{S^2\sigma}{\kappa}T \tag{17}$$

and plotted against temperature as presented in Figure 9d. The 18 m/o FeO$_{1.5}$-doped ZnO sample annealed at 1350 °C has the best power factor and figure of merit significantly superior to other samples over the medium to high temperature range. Compared to other element-doped ZnO systems, it has relatively higher power factor or ZT value than Ga-doped ZnO[52] and In and Ga dually doped ZnO,[18] similar thermoelectric performance to Sb-[15] or Sn[16]-doped ZnO, while lower than the Al-[53] or In[50]-doped ZnO and Al and Ga dually doped ZnO.[54] Nevertheless, the Fe–ZnO system has the great advantage of achieving the refined nanostructures through high temperature treatment, which is essential to maintain good thermoelectric properties at high temperatures.

CONCLUSIONS

Systematic studies were made correlating the thermoelectric properties with phase and microstructure change of Fe-doped ZnO materials. The Fe content in ZnO solid solution phase is strongly dependent on phase equilibria. Both thermal and electrical conductivity are observed to be sensitive to the actual Fe concentration in the ZnO phase. By properly choosing the composition and annealing temperature, the Fe highly concentrated ZnO solid solution phase can be produced, which significantly improves the overall thermoelectric properties by reducing thermal conductivity and enhancing electrical conductivity.

By analyzing the temperature measurements of Seebeck coefficients combined with an application of mixture law, we were able to estimate the Fermi level in the constituting phases of the materials. The Fermi level in all the samples were found to be below the conduction band suggesting that they remain as degenerate semiconductors, even with large addition of FeO$_{1.5}$ up to 18 m/o.

All the samples investigated in the current work demonstrate free electron semiconductor behavior, as analyzed by a Jonker plot. The maximum achievable power factor of Fe-doped ZnO was estimated and comparable to that of the ZnO–In$_2$O$_3$ system. An unusual high-temperature nanostructure refinement was found in 18 m/o FeO$_{1.5}$-doped ZnO, which suggests that Fe-doped ZnO can be a potential high-temperature thermoelectric material.

AUTHOR INFORMATION

Corresponding Author
*E-mail: liangxin_mse@163.com.

Present Address
‡School of Materials Science and Engineering, Changzhou University, Changzhou, Jiangsu 213164, China.

Notes
The authors declare no competing financial interest.

REFERENCES

(1) Tsubota, T.; Ohtaki, M.; Eguchi, K.; Arai, H. Thermoelectric Properties of Al-doped ZnO as a Promising Oxide Material for High-temperature Thermoelectric Conversion. *J. Mater. Chem.* **1997**, *7*, 85−90.

(2) Fujishiro, Y.; Miyata, M.; Awano, M.; Maeda, K. Effect of Microstructural Control on Thermoelectric Properties of Hot-Pressed Aluminum-Doped Zinc Oxide. *J. Am. Ceram. Soc.* **2003**, *86*, 2063−2066.

(3) Park, K.; Choi, J. W.; Kim, S. J.; Kim, G. H.; Cho, Y. S. Zn$_{1-x}$Bi$_x$O (0 < x<0.02) for Thermoelectric Power Generations. *J. Alloys Compd.* **2009**, *485*, 532−537.

(4) White, M. A.; Ochsenbein, S. T.; Gamelin, D. R. Colloidal Nanocrystals of Wurtzite Zn$_{1-x}$Co$_x$O (0 <x <1): Models of Spinodal Decomposition in an Oxide Diluted Magnetic Semiconductor. *Chem. Mater.* **2008**, *20*, 7107−7116.

(5) Ohta, H.; Seo, W. S.; Koumoto, K. Thermoelectric Properties of Homologous Compounds in the ZnO-In$_2$O$_3$ System. *J. Am. Ceram. Soc.* **1996**, *79*, 2193−2196.

(6) Kazeoka, M.; Hiramatsu, H.; Seo, W. S.; Koumoto, K. Improvement in Thermoelectric Properties of (ZnO)$_5$In$_2$O$_3$ through Partial Substitution of Yttrium For Indium. *J. Mater. Res.* **1998**, *13*, 523−526.

(7) Orikasa, Y.; Hayashi, N.; Muranaka, S. Effects of Oxygen Gas Pressure on Structural, Electrical, And Thermoelectric Properties of (ZnO)$_3$In$_2$O$_3$ Thin Films Deposited by Rf Magnetron Sputtering. *J. Appl. Phys.* **2008**, *103*, 7.

(8) Hopper, E. M.; Zhu, Q. M.; Song, J. H.; Peng, H. W.; Freeman, A. J.; Mason, T. O. Electronic and Thermoelectric Analysis of Phases in the In$_2$O$_3$(ZnO)$_k$ System. *J. Appl. Phys.* **2011**, *109*, 6.

(9) Peng, H. W.; Song, J. H.; Hopper, E. M.; Zhu, Q. M.; Mason, T. O.; Freeman, A. J. Possible n-type Carrier Sources in In$_2$O$_3$(ZnO)$_k$. *Chem. Mater.* **2012**, *24*, 106−114.

(10) Li, C.; Bando, Y.; Nakamura, M.; Kimizuka, N. Antiphase Modulated Structure of Fe$_2$O$_3$(ZnO)$_{15}$ Studied by High-Resolution Electron Microscopy. *J. Solid State Chem.* **1999**, *142*, 174−179.

(11) Köster-Scherger, O.; Schmid, H.; Vanderschaeghe, N.; Wolf, F.; Mader, W. ZnO with Additions of Fe$_2$O$_3$: Microstructure, Defects, and Fe Solubility. *J. Am. Ceram. Soc.* **2007**, *90*, 3984−3991.

(12) Li, X.; Yu, Z.; Long, X.; Lin, P.; Cheng, X.; Liu, Y.; Cao, C.; Zhang, H.; Wu, G.; Yu, R. Synthesis and Magnetic Properties of Al Doped Zn$_{0.995}$Mn$_{0.005}$O Powers. *Appl. Phys. Lett.* **2009**, *94*, 252501.

(13) Park, K.; Seong, J. K.; Kim, G. H. NiO Added Zn$_{1-x}$Ni$_x$O (0 < x<0.05) for Thermoelectric Power Generation. *J. Alloys Compd.* **2009**, *473*, 423−427.

(14) Colder, H.; Guilmeau, E.; Harnois, C.; Marinel, S.; Retoux, R.; Savary, E. Preparation of Ni-doped ZnO Ceramics for Thermoelectric Applications. *J. Eur. Ceram. Soc.* **2011**, *31*, 2957−2963.

(15) Park, K.; Seong, J. K.; Nahm, S. Improvement of Thermoelectric Properties with the Addition of Sb to ZnO. *J. Alloys Compd.* **2008**, *455*, 331−335.

(16) Park, K.; Seong, J. K.; Kwon, Y.; Nahm, S.; Cho, W. S. Influence of SnO$_2$ Addition on the Thermoelectric Properties of Zn$_{1-x}$Sn$_x$O (0.01 ≤ x ≤ 0.05). *Mater. Res. Bull.* **2008**, *43*, 54−61.

(17) Park, K.; Seong, J. K. Influence of Simultaneous Addition of Sb$_2$O$_3$ and SnO$_2$ on Thermoelectric Properties of Zn$_{1-x-y}$Sb$_x$Sn$_y$O Prepared by Tape Casting. *J. Alloys Compd.* **2008**, *464*, 1−5.

(18) Seo, D. K.; Shin, S.; Cho, H. H.; Kong, B. H.; Whang, D. M.; Cho, H. K. Drastic Improvement of Oxide Thermoelectric Performance Using Thermal and Plasma Treatments of the InGaZnO Thin Films Grown by Sputtering. *Acta Mater.* **2011**, *59*, 6743−6750.

(19) Yamaguchi, H.; Chonan, Y.; Oda, M.; Komiyama, T.; Aoyama, T.; Sugiyama, S. Thermoelectric Properties of ZnO Ceramics Co-

Doped with Al and Transition Metals. *J. Electron. Mater.* **2011**, *40*, 723−727.

(20) Liu, H.; et al. Structure and Magnetic Properties of Fe-doped ZnO Prepared by the Sol-gel Method. *J. Phys.: Condens. Matter* **2009**, *21*, 145803.

(21) Liu, H.; et al. Structure, Magnetic, and Optical Properties in $Zn_{0.98}Cu_{0.02}Fe_xO$ Diluted Magnetic Semiconductors. *Phys. Status Solidi A* **2010**, DOI: 10.1002/pssa.200925456.

(22) Degterov, S. A.; Jak, E.; Hayes, P. C.; Pelton, A. D. Experimental Study of Phase Equilibria and Thermodynamic Optimization of the Fe-Zn-O System. *Metall. Mater. Trans. B* **2001**, *32*, 643−657.

(23) ICDD Database. International Centre for Diffraction Data: Newtown Square, PA, 2011.

(24) Barin, I. *Thermochemical Data of Pure Substances;* VCH: Weinheim, Germany, 1989.

(25) Yamashita, T.; Hansson, R.; Hayes, P. C. The Relationships between Microstructure and Crystal Structure in Zincite Solid Solutions. *J. Mater. Sci.* **2006**, *41*, 5559−5568.

(26) Nakamura, M.; Kimizuka, N.; Mohri, T. The Phase Relations in the In_2O_3-Fe_2ZnO_4-ZnO System at 1350 Degree C. *J. Solid State Chem.* **1990**, *86*, 16−40.

(27) Kimizuka, N.; Isobe, M.; Nakamura, M.; Mohri, T. Syntheses and Crystallographic Data of the Homologous Compounds $InFeO_3(ZnO)_m$ (m = 1, 2, 3, 7, 11, 13, 15, and 19) and $Fe_2O_3(ZnO)_m$ (m = 8 and 9) in the In_2O_3-$ZnFe_2O_4$-ZnO System. *J. Solid State Chem.* **1993**, *103*, 394−402.

(28) Kimizuka, N.; Isobe, M.; Nakamura, M.; Mohri, T. Syntheses and Crystallographic Data of the Homologous Compounds InFeO3-(ZnO)m, (m = 1, 2, 3, 7, 11, 13, 15, and 19) and Fe2O3(ZnO)m (m = 8 and 9) in the In2O3-ZnFe2O4-ZnO System. *J. Solid State Chem.* **1993**, *103*, 394−402.

(29) Uchida, N.; Bando, Y.; Nakamura, M.; Kimizuka, N. High-resolution Electron-microscopy of Homologous Compounds In-$FeO_3(ZnO)_m$. *J. Electron Microsc.* **1994**, *43*, 146−150.

(30) Zhou, S. Q.; Potzger, K.; Reuther, H.; Talut, G.; Eichhorn, F.; von Borany, J.; Skorupa, W.; Helm, M.; Fassbender, J. Crystallographically Oriented Magnetic $ZnFe_2O_4$ Nanoparticles Synthesized by Fe Implantation into ZnO. *J. Phys. D: Appl. Phys.* **2007**, *40*, 964−969.

(31) Kingery, W. D. *Introuduction to Ceramics,* 2nd ed.; Wiley Interscience: New York, 1976.

(32) Callaway, J.; von Baeyer, H. C. Effect of Point Imperfections on Lattice Thermal Conductivity. *Phys. Rev.* **1960**, *120*, 1149−1154.

(33) Qu, Z.; Sparks, T. D.; Pan, W.; Clarke, D. R. Thermal Conductivity of the Gadolinium Calcium Silicate Apatites: Effect of Different Point Defect Types. *Acta Mater.* **2011**, *59*, 3841−3850.

(34) Sultan, M.; Singh, R. Structural and Optical Properties of RF-sputtered $ZnFe_2O_4$ Thin Films. *J. Phys. D: Appl. Phys.* **2009**, *42*, 115306.

(35) Johnson, V. A.; Lark-Horovitz, K. Theory of Thermoelectric Power in Semiconductors with Applications to Germanium. *Phys. Rev.* **1953**, *92*, 226−232.

(36) Fritzsche, H. A General Expression for the Thermoelectric Power. *Solid State Commun.* **1971**, *9*, 1813−1815.

(37) Ambia, M. G.; Islam, M. N.; Hakim, M. O. Studies on the Seebeck Effect in Semiconducting ZnO Thin Films. *J. Mater. Sci.* **1992**, *27*, 5169−5173.

(38) Ko, D.-K.; Urban, J. J.; Murray, C. B. Carrier Distribution and Dynamics of Nanocrystal Solids Doped with Artificial Atoms. *Nano Lett.* **2010**, *10*, 1842−1847.

(39) Ko, D. K.; Murray, C. B. Probing the Fermi Energy Level and the Density of States Distribution in PbTe Nanocrystal (Quantum Dot) Solids by Temperature-Dependent Thermopower Measurements. *ACS Nano* **2011**, *5*, 4810−4817.

(40) Emin, D. Effect of Temperature-Dependent Band Shifts on Semiconductor Transport Properties. *Solid State Commun.* **1977**, *22*, 409−411.

(41) Nguyen, T. H.; O'Leary, S. K. The Dependence of the Fermi Level on Temperature, Doping Concentration, and Disorder in Disordered Semiconductors. *J. Appl. Phys.* **2000**, *88*, 3479−3483.

(42) Janotti, A.; Walle, C. G. V. d. Fundamentals of Zinc Oxide as a Semiconductor. *Rep. Prog. Phys.* **2009**, *72*, 126501.

(43) Bergman, D. J.; Fel, L. G. Enhancement of Thermoelectric Power Factor in Composite Thermoelectrics. *J. Appl. Phys.* **1999**, *85*, 8205−8216.

(44) Kleber, X.; Simonet, L.; Fouquet, F. A Computational Study of the Thermoelectric Power of 2D Two Phase Materials. *Modell. Simul. Mater. Sci. Eng.* **2006**, *14*, 21.

(45) Jonker, G. H. Application of Combined Conductivity and Seebeck-Effect Plots For Analysis of Semiconductor Properties. *Philips Res. Rep.* **1968**, *23*, 131−&.

(46) Hopper, E. M.; Zhu, Q. M.; Song, J. H.; Peng, H. W.; Freeman, A. J.; Mason, T. O. Electronic and Thermoelectric Analysis of Phases in the $In_2O_3(ZnO)_k$ System. *J. Appl. Phys.* **2011**, *109*.

(47) Zhu, Q. M.; Hopper, E. M.; Ingram, B. J.; Mason, T. O. Combined Jonker and Ioffe Analysis of Oxide Conductors and Semiconductors. *J. Am. Ceram. Soc.* **2011**, *94*, 51−57.

(48) Ashcroft, N. W.; David, M. N. *Solid State Physics;* Thomson: Stamford, CT, 1976.

(49) Tritt, T. M. Thermoelectric Phenomena, Materials, and Applications. In *Annual Review of Materials Research;* Clarke, D. R., Fratzl, P., Eds.; **2011**; Vol. *41*, pp 433−448.

(50) Liang, X.; Clarke, D. R. Relation Between Thermoelectric Properties and Phase Equilibria in the $ZnO-In_2O_3$ Binary System. *Acta Mater.* **2014**, *63*, 191−201.

(51) Ioffe, A. F. *Semiconductor Thermoelements and Thermoelectric Cooling;* Infosearch Ltd.: London, U.K., 1957.

(52) Michiue, Y.; Mori, T.; Prytuliak, A.; Matsushita, Y.; Tanaka, M.; Kimizuka, N. Electrical, Optical, and Thermoelectric Properties of $Ga_2O_3(ZnO)_9$. *RSC Adv.* **2011**, *1*, 1788−1793.

(53) Jood, P.; Mehta, R. J.; Zhang, Y.; Peleckis, G.; Wang, X.; Siegel, R. W.; Borca-Tasciuc, T.; Dou, S. X.; Ramanath, G. Al-Doped Zinc Oxide Nanocomposites with Enhanced Thermoelectric Properties. *Nano Lett.* **2011**, *11*, 4337−4342.

(54) Ohtaki, M.; Araki, K.; Yamamoto, K. High Thermoelectric Performance of Dually Doped ZnO Ceramics. *J. Electron. Mater.* **2009**, *38*, 1234−1238.